Astron. Astrophys. 336, 1029–1038 (1998)

ASTRONOMY AND ASTROPHYSICS

The heating of solar magnetic flux tubes

I. Adiabatic longitudinal tube waves

Diaa E. Fawzy[1], **P. Ulmschneider**[1], **and M. Cuntz**[2,1]

[1] Institut für Theoretische Astrophysik der Universität Heidelberg, Tiergartenstr. 15, D-69121 Heidelberg, Germany
[2] Center for Space Plasma, Aeronomy, and Astrophysics Research (CSPAAR), TH S101, University of Alabama in Huntsville, Huntsville, AL 35899, USA

Received 30 October 1997 / Accepted 5 May 1998

Abstract. We study the formation of shocks and shock heating by adiabatic longitudinal tube waves in solar magnetic flux tubes of different shape. Monochromatic waves with periods between 20 and 160 s and energy fluxes ranging from $1 \cdot 10^7$ to $1 \cdot 10^9$ erg cm^{-2}s^{-1} were considered. It is found that the tube shape is of critical importance for the heating of flux tubes. Constant cross-section tubes show large heating, whereas exponentially spreading tubes show little or no heating at all. In tubes of intermediate shapes ("wine-glass tubes"), the heating is essentially restricted to those regions, where the tube has attained its maximum diameter. This finding is in good agreement with the observation that the chromospheric network can still be seen well above the canopy height. In tubes of lower field strength, the shock formation is delayed and heating is reduced.

Key words: magnetohydrodynamics (MHD) – shock waves – waves – Sun: chromosphere – Sun: magnetic fields – Sun: photosphere

1. Introduction

Observations of the Sun's photosphere show that isolated small-scale magnetic flux tubes occur in the chromospheric network regions between the supergranules. One finds that the flux tubes are magnetically strong, with fields of about 1.5 kG and are confined to radii of about 100 km (see e.g. Stenflo 1978, 1989, 1994; Zwaan 1978; Solanki 1990, 1993, 1997; Schüssler 1991; Wang et al. 1996; Hasan & van Ballegooijen 1997). These magnetic tubes are thought to extend and to spread in pressure equilibrium through the chromosphere and beyond a merging height up into the corona, which is completely filled by magnetic fields. Here the magnetized plasma regions form coronal loops, which are regions of high gas density, although temperature and magnetic field strength differ in space and time.

Magnetic flux tubes also operate as communication channels, linking one part of the Sun's atmosphere to another. Their essential one-dimensionality means that the linkage is likely to be efficient for momentum and energy transport, allowing flows and waves to be carried from one side to another. Magnetoacoustic wave propagation in thin photospheric magnetic flux tubes has been extensively studied in the last two decades particularly in the case of negligible gravity (Defouw 1976; Roberts & Webb 1978, 1979; Webb & Roberts 1980; Wilson 1979, 1980, 1981; Parker 1979; Wentzel 1979; Spruit 1981a,b, 1982; see also reviews by Spruit & Roberts 1983; Thomas 1985; Hollweg 1986, 1990; Roberts 1981, 1991, Edwin & Roberts 1983; Ryutova 1990; Roberts & Ulmschneider 1997). The treatment of wave propagation usually starts from the linearized MHD equations valid for specified tube geometries. In case of zero gravity, the wave equation is solved for a wave moving along the vertically-directed tube axis. The horizontal variation of the physical quantities is described by Bessel functions both inside and outside the tube. Suitable matching at the tube boundary allows the construction of complete wave solutions. There are several types of wave modes possible (see Spruit 1982; Edwin & Roberts 1983): the torsional mode, kink modes, and the longitudinal mode.

Of these modes the longitudinal tube wave is the only one being compressive. Because of this property it closely resembles acoustic tube waves travelling in rigid funnels. There is also a close similarity to plane acoustic waves. For situations of non-negligible gravity, these waves have first been studied by Defouw (1976), who assumed an isothermal atmosphere. This study was subsequently generalized by Roberts & Webb (1978) to non-isothermal atmospheres. In both investigations the pressure perturbation and thus the waves in the medium outside the flux tube were neglected to make the problem feasible.

While Rae & Roberts (1982) and Roberts (1981, 1983) studied linear longitudinal tube waves, Herbold et al. (1985) extended that work to the non-linear regime and also investigated shock formation, which allowed a realistic representation of the heating. The shock formation property of longitudinal tube waves is particularly relevant for the problem of chromospheric and coronal heating. Observations of solar and stellar UV, EUV and X-ray fluxes (e.g., Linsky 1980; Vaiana et al. 1981) have shown that for chromospheres and coronae of rapidly rotating stars magnetic heating mechanisms must be present. A theo-

Send offprint requests to: P. Ulmschneider
Correspondence to: ulmschneider@ita.uni-heidelberg.de

retical study of chromospheric heating based on longitudinal tube waves for magnetically active K2 V stars with different rotation periods was recently given by Cuntz et al. (1998). This work shows that fast rotating stars have considerably increased wave energy dissipation rates particularly in the high and middle chromosphere, which can likely explain the increased Ca II and Mg II emission (and that of other emission lines as well) observed in magnetically active main-sequence stars.

A review of chromospheric and coronal heating mechanisms suggests that longitudinal tube waves are a prime candidate for the heating of magnetic chromospheres (Narain & Ulmschneider 1990, 1996). This is also suggested by the close similarity to acoustic waves, which Buchholz & Ulmschneider (1994) and Buchholz et al. (1998) identified as the dominant heating mechanism outside magnetic regions. Carlsson & Stein (1992) also showed that acoustic energy dissipation in the solar internetwork regions is capable of reproducing the observed temporal variations in the Ca II K line profile including the wing brightening pattern, the violet/red peak asymmetry and the line center Doppler shift, which is further evidence for acoustic heating in non-magnetic solar regions.

It is noteworthy that the close similarity between acoustic waves and longitudinal tube waves does not just concern the heating and the shock formation properties, but also the way these different types of waves are generated in the stellar convection zone (Musielak et al. 1989, 1994, 1995; Huang et al. 1995; Ulmschneider & Musielak 1998). Although tube wave generation calculations show that the fluxes of transverse waves are more than an order of magnitude higher than the longitudinal wave fluxes, the former appear to suffer much more from energy leakage from the tube. This result has been found in recent 3-D wave computations of Ziegler & Ulmschneider (1997a,b). Because of the known difficulty of dissipating Alfvén waves, it thus seems very reasonable that longitudinal tube waves should be considered the main heating mechanism of chromospheric flux tubes up to the level of Mg II and Ca II line core emission. Alfvén waves may then become a main heating agent in the highest chromospheric layers, the transition region as well as in the corona, where that mechanism is joined by microflare and nanoflare heating (see Narain & Ulmschneider 1996). This picture of a combined wave plus flare heating mechanism of the transition layer plus corona is also supported by recent semiempirical studies of Wood et al. (1997) and Judge et al. (1998).

It is the aim of this series of papers to study the wave propagation and shock heating properties of *longitudinal tube waves* in detail. In the present paper we investigate the shock formation and shock propagation of *adiabatic* longitudinal waves in the flux tube environment. In particular, we concentrate on the dependence of heating on the tube geometry and the wave period. Sect. 2 summarizes our numerical methods, Sect. 3 presents the results and Sect. 4 gives the conclusions.

2. Method

2.1. Magnetohydrodynamic equations

We consider a thin, vertically oriented magnetic flux tube in the solar atmosphere which is embedded in a non-magnetic external medium. Following Defouw (1976), Roberts & Webb (1979) as well as Herbold et al. (1985) the magnetohydrodynamic equations in the thin flux tube approximation can be written

$$\frac{\partial}{\partial t}\left(\frac{\rho}{B}\right)+\frac{\partial}{\partial z}\left(\frac{\rho u}{B}\right)=0\,, \tag{1}$$

$$\frac{\partial u}{\partial t}+u\frac{\partial u}{\partial z}+\frac{1}{\rho}\frac{\partial p}{\partial z}+g=0\,, \tag{2}$$

$$p+\frac{B^2}{8\pi}=p_e\left(z\right)\,, \tag{3}$$

$$\frac{\partial S}{\partial t}+u\frac{\partial S}{\partial z}=\left.\frac{dS}{dt}\right|_{Rad}\,. \tag{4}$$

In our present adiabatic calculations we set $dS/dt|_{Rad}=0$, while in subsequent work we will consider radiation damping $dS/dt|_{Rad}\neq 0$. In the thin tube approximation the tube is seen as a slender string of mass elements where the variations of the physical quantities across the tube are assumed to be small. Hence, the state of each mass element can be given by the single values ρ, p, S, u and B at the tube axis. Here ρ is the density, p the gas pressure, S the entropy, u the gas velocity, and B the magnetic field strength. All these variables are functions of height z and time t. Any wave disturbance traveling along the tube is assumed not to perturb the outside atmosphere. Therefore, the gas pressure outside the tube p_e is assumed to be a function of z only. At this point we must stress that the thin tube approximation assumption must be further tested by detailed 2-D and 3-D MHD computations. Theoretical work by Huang (1996) on 2-D slabs akin to solar flux tubes indicates that for longitudinal tube waves the energy leakage is relatively small and thus the thin tube approximation is acceptable.

The four Eqs. (1) to (4) are sufficient to compute the five quantities ρ, p, S, u and B, because only two of the three thermodynamic variables are independent. We now eliminate B from the system by using Eqs. (1) and (3). From (1) we get

$$\frac{\partial \rho}{\partial t}-\frac{\rho}{B}\frac{\partial B}{\partial t}+\rho\frac{\partial u}{\partial z}+u\frac{\partial \rho}{\partial z}-\frac{\rho u}{B}\frac{\partial B}{\partial z}=0\,, \tag{5}$$

while from (3) we have

$$\frac{1}{B}\frac{\partial B}{\partial t}=-\frac{8\pi}{2B^2}\frac{\partial p}{\partial t}=-\frac{1}{\rho c_A^2}\frac{\partial p}{\partial t}\,, \tag{6}$$

$$\frac{1}{B}\frac{\partial B}{\partial z}=\frac{8\pi}{2B^2}\left(\frac{dp_e}{dz}-\frac{\partial p}{\partial z}\right)=\frac{1}{\rho c_A^2}\left(\frac{dp_e}{dz}-\frac{\partial p}{\partial z}\right)\,, \tag{7}$$

where

$$c_A=\frac{B}{\sqrt{4\pi\rho}} \tag{8}$$

is the Alfvén speed. With (6) and (7), the B derivatives in (5) can be replaced and one obtains

$$\frac{\partial \rho}{\partial t}+\frac{1}{c_A^2}\frac{\partial p}{\partial t}+\rho\frac{\partial u}{\partial z}+u\frac{\partial \rho}{\partial z}-\frac{u}{c_A^2}\left(\frac{dp_e}{dz}-\frac{\partial p}{\partial z}\right)=0\ . \quad (9)$$

The system (1) to (4) is now reduced to the three differential equations (2), (4) and (9) for the unknowns ρ, p, S and u. We also must compute the thermodynamic variables temperature T and adiabatic sound speed c_S. Only two of the thermodynamic variables are independent. We thus express all thermodynamic variables by the variables c_S and S. The relationship between the thermodynamic variables is given by the ideal gas law

$$p=\rho\frac{\Re T}{\mu} \quad (10)$$

and

$$c_S^2=\gamma\frac{\Re T}{\mu}=\gamma\frac{p}{\rho}\ , \quad (11)$$

where γ is the ratio of specific heats, μ the molecular weight, and $\Re$ the gas constant. Combining the first and second law of thermodynamics yields

$$\frac{d\rho}{\rho}=\frac{2}{\gamma-1}\frac{dc_S}{c_S}-\frac{\mu}{\Re}dS\ , \quad (12)$$

$$\frac{dp}{p}=\frac{2\gamma}{\gamma-1}\frac{dc_S}{c_S}-\frac{\mu}{\Re}dS\ . \quad (13)$$

Using the above relations, Eqs. (2), (4) and (9) can now be written as a system of three partial differential equations for the three unknowns c_S, S and u. To employ the method of characteristics we transform this system of three partial differential equations into a system of six ordinary differential equations defined along the characteristic lines. We obtain the two compatibility relations

$$du\pm\frac{2}{\gamma-1}\frac{c_S}{c_T}dc_S\mp\frac{\mu c_S}{\gamma\Re}\frac{c_S}{c_T}dS\mp\frac{\mu c_T(\gamma-1)}{\gamma\Re}\left.\frac{dS}{dt}\right|_{Rad}dt$$
$$\mp\frac{uc_T}{\rho c_A^2}\frac{dp_e}{dz}dt+gdt=0\ , \quad (14)$$

along the C^+ and C^- characteristics given by

$$\frac{dz}{dt}=u\pm c_T\ , \quad (15)$$

where the upper (lower) sign corresponds to the C^+ (C^-) characteristic. The tube speed c_T is given by

$$\frac{1}{c_T^2}=\frac{1}{c_S^2}+\frac{1}{c_A^2}\ . \quad (16)$$

Eqs. (14) and (15) are four ordinary differential equations. The two remaining ordinary differential equations are obtained from (4) written in characteristic form

$$dS=\left.\frac{dS}{dt}\right|_{Rad}dt \quad (17)$$

along the (fluid path) C^0 characteristic

$$\frac{dz}{dt}=u\ . \quad (18)$$

2.2. Shocks

During propagation longitudinal tube waves form shocks due to the density gradient. At the shocks we have the variables ρ_1, p_1, c_{S1}, S_1, u_1, A_1, $H_1=\gamma p_1/((\gamma-1)\rho_1)$ in front of the shock and corresponding variables with index 2 behind the shock. Here H_1 is the enthalpy and A_1 the tube cross-section. The Rankine-Hugoniot relations for longitudinal tube waves can be written (Herbold et al. 1985)

$$\rho_1 v_1 A_1=\rho_2 v_2 A_2\ , \quad (19)$$

$$A_1\left(\rho_1 v_1^2-2p_e+2p_1\right)=A_2\left(\rho_2 v_2^2-2p_e+2p_2\right)\ , \quad (20)$$

$$\frac{1}{2}v_1^2+H_1=\frac{1}{2}v_2^2+H_2\ , \quad (21)$$

where v_1, v_2 are the gas velocities in the shock frame. The transformation of the gas velocity from the laboratory (Euler) frame into the shock frame is accomplished by

$$v_1=u_1-U_{SH}\ ,\quad v_2=u_2-U_{SH}\ , \quad (22)$$

where U_{SH} is the shock velocity in the laboratory frame. The Rankine-Hugoniot relations are solved by assuming that the front shock state is known and by specifying a post-shock velocity u_2. The front shock state is updated through the iteration process for the respective hydrodynamic time-step. With $\Delta u=u_2-u_1$ and known quantities in front of the shock the cubic equation

$$E_0+E_1A_2+E_2A_2^2+E_3A_2^3=0\ , \quad (23)$$

with

$$E_0=\frac{\gamma-2}{\gamma-1}A_1^2\ , \quad (24)$$

$$E_1=A_1\left[\frac{4-3\gamma}{\gamma-1}-\frac{4\pi}{\Phi^2}\Delta u^2\rho_1\frac{A_1^2}{\gamma-1}-\frac{8\pi}{\Phi^2}H_1\rho_1A_1^2\right]\ , \quad (25)$$

$$E_2=2-\frac{4\pi}{\Phi^2}\Delta u^2\rho_1A_1^2+\frac{\gamma}{\gamma-1}\frac{8\pi}{\Phi^2}p_eA_1^2+\frac{8\pi}{\Phi^2}H_1\rho_1A_1^2, \quad (26)$$

$$E_3=\frac{\gamma}{\gamma-1}\frac{8\pi}{\Phi^2}p_eA_1\left[\frac{4\pi}{\Phi^2}\Delta u^2\rho_1A_1^2-1\right]\ , \quad (27)$$

is solved for A_2 by using a Newton-Raphson iteration scheme. Here $\Phi=A_1B_1$ is the magnetic flux. The other post-shock quantities are then computed using

$$\rho_2=\frac{\rho_1\frac{A_1}{A_2}(A_1-A_2)}{\frac{4\pi}{\Phi^2}\Delta u^2\rho_1A_1^2A_2+A_1-A_2}\ , \quad (28)$$

$$v_2=\frac{\rho_1A_1\Delta u}{\rho_2A_2-\rho_1A_1}\ , \quad (29)$$

$$U_{SH}=u_2-v_2\ , \quad (30)$$

$$p_2=p_e-\frac{\Phi^2}{8\pi A_2^2}\ , \quad (31)$$

$$c_{S2} = \sqrt{\gamma \frac{p_2}{\rho_2}}\,, \tag{32}$$

and

$$S_2 = S_1 + \Delta S = S_1 + \frac{\Re}{\mu} \log \left(\frac{v_2 A_2}{v_1 A_1} \left(\frac{c_{S2}}{c_{S1}} \right)^{2/(\gamma-1)} \right). \tag{33}$$

2.3. Flux tube models

In our investigation we consider three different magnetic flux tube models. We start by constructing a non-grey radiative and hydrostatic equilibrium solar atmosphere model with an effective temperature $T_{\rm eff} = 5770$ K and gravity $g = 2.736 \cdot 10^4$ cm s^{-2} using the temperature and flux correction procedure of Cuntz et al. (1994). In this model, NLTE H^- continuum and Mg II *k* line cooling have been assumed. The atmosphere has a temperature which continuously decreases in outward direction and there is no mechanical heating. Magnetic flux tubes are subsequently embedded in this atmosphere. At height $z = 0$, where in the external atmosphere the optical depth is $\tau_{5000} = 1$, the tubes have a specified radius $r_B = 50$ km and a magnetic field strength B_0. The tubes are allowed to spread with height in pressure balance with the surrounding gas pressure (cf. Eq. 3) up to a height z_H. The spreading rate from height z_H to the maximum height $z_T = 2000$ km is chosen differently for the different tube models.

The case with $z_H = z_T$ is called *exponential tube*. For the so-called *wine-glass tube* model we have $z_H < z_T$. Here for the heights $z \geq z_H$ we fit a radius function $r = (r_T - r_H)\sin(2\pi(z - z_H)/L)$, which ensures that the slope dr/dz at z_H is continuous and that the tube approaches a specified radius r_T at great height. r_H is the radius at z_H and L is determined by the slope at z_H. To ensure that the tube has this specified radius, an additional time-independent external pressure is assumed, which is supposed to originate from magnetic interaction with neighboring tubes. The gas pressure in the tube is computed in hydrostatic equilibrium and the temperature is determined by radiative equilibrium using the above-mentioned temperature correction procedures. Choosing $z_H = 0$ and $r_T = r_B$ leads to our third tube model, the *constant cross-section tube*. For the wine-glass tube, we take $z_H = 400$ km and $r_T = 300$ km. The three types of tubes obtained are displayed in Fig. 1.

The exponential tube with its unobstructed spreading may be typical for tubes in the interior of supergranulation cells or in areas just outside the network region, while the constant cross-section tube may be representative for the inner part of a very crowded network region. The wine-glass tube with a filling factor $f = r_B^2/r_T^2 \approx 2.8\%$ thus corresponds to the situation at the outer parts of a normal network region (Solanki 1997, private communication).

2.4. Wave computations

Using a time-dependent magnetohydrodynamic wave code (Herbold et al. 1985; Zhugzhda et al. 1995) various monochromatic waves with periods P and wave energy fluxes F_M were introduced at height z_B at the bottom of the tube by means of a piston. The values of P and F_M have been varied to present a set of case studies. The piston velocity u is prescribed by

$$u(t) = u_0 \, \sin\left(\frac{2\pi}{P} t\right) \quad , \quad u_0 = \sqrt{\frac{2F_{\rm M}}{\rho_0 c_{T0}}}\,, \tag{34}$$

where u_0 is the velocity amplitude. Here ρ_0 and c_{T0} are the density in the tube and the tube speed at height $z = z_B = 0$. During the propagation, shocks form, which are treated as discontinuities and permitted to grow to arbitrary strength and to merge. The positions of shock formation are found by monitoring intersection points of adjacent C^+ characteristics.

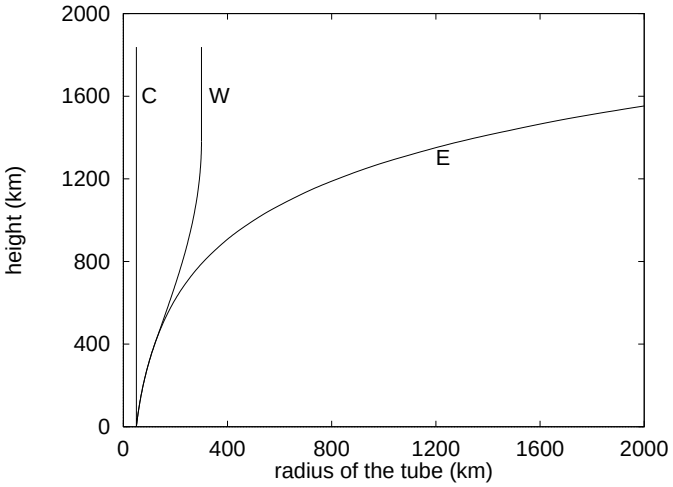

Fig. 1. Shape of the exponential (E), constant cross-section (C), and wine-glass (W) magnetic flux tubes as used in the present work. The radii of the tubes are shown as function of height.

3. Results

3.1. Varying the tube shape and the wave period

For the various prescribed wave periods P and wave fluxes F_M, adiabatic monochromatic longitudinal waves are introduced into our three tube models at the bottom by means of a piston using the velocity function of Eq. (34). These waves propagate along the tubes and quickly develop into sawtooth shape leading to the formation of shocks. By shock dissipation, they heat the tubes to chromospheric temperatures.

As our calculations are adiabatic, the deposited wave energy cannot be radiated away. This leads to a perpetual increase of the local temperature. That is because for every passage of a shock, the local entropy at a given mass element is increased by the entropy-jump ΔS, given by Eq. (33), which leads to a perpetual increase of the mean temperature in the regions where shock dissipation occurs. Fig. 2 shows the height dependence of the mean temperature for waves with the same wave flux $F_M = 1 \cdot 10^7$ erg cm^{-2}s^{-1} and various periods $P = 20, 40, 80, 160$ s in the three tube models. The mean temperatures (averaged over 400 s) are shown every 400 s, marked $0, 1, 2, \ldots$ The figure

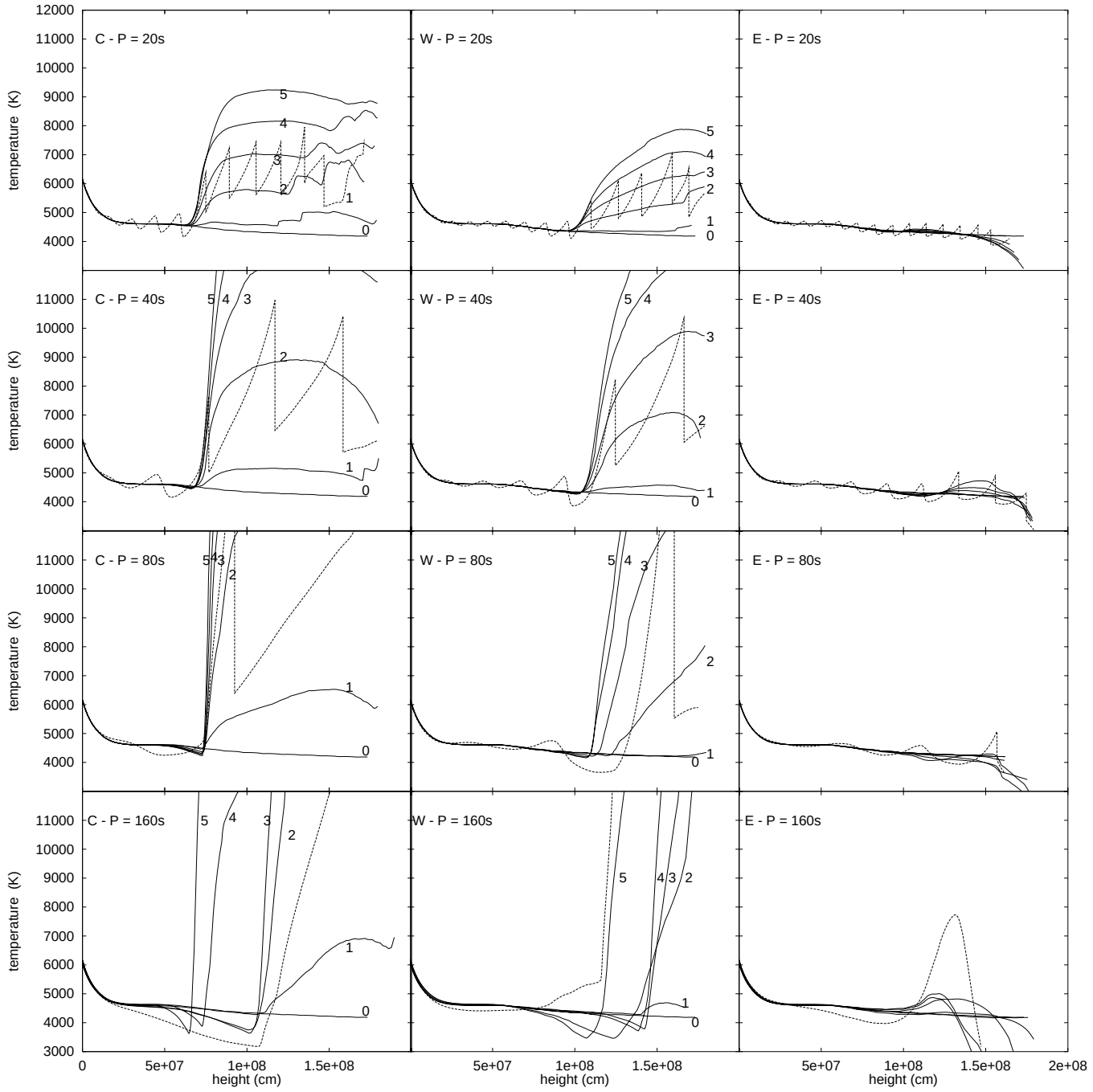

Fig. 2. Height dependence of the mean temperature (solid) for waves with the same energy flux $F_M = 1 \cdot 10^7$ erg cm^{-2}s^{-1} and periods $P = 20,\ 40,\ 80,\ 160$ s (from top to bottom) for the three tube models. The left column shows the constant cross-section tube (C), the middle column shows the wine-glass tube (W), and the right column shows the exponential tube (E). The mean temperatures are shown in 400 s intervals (marked by 1, 2, 3, 4, 5, respectively) starting from $t = 400$ s up to the time $t = 2000$ s. Also shown are the initial temperature distribution (marked 0) and the instantaneous temperature at $t = 800$ s (dashed).

also shows the temperature of the initial atmosphere and the instantaneous temperature at time $t = 800$ s.

Let us first discuss the *constant cross-section tube* cases (left column). In all four wave cases it is seen that the mean temperatures perpetually increase with time. The behaviour of the instantaneous temperature shows that this rise of the mean temperatures occurs only at heights where shocks have formed and have become fully developed, i.e., where shock dissipation is significant. Because the shock strength grows almost linearly with the wave period and as the entropy-jump depends roughly on the third power of the shock amplitude, the heating is stronger for larger wave period. Fig. 2 also shows that for a given wave

period, the magnitudes of the temperature-jumps at the shocks do not depend on height after the shocks are fully developed. This is also a well-known property of acoustic waves and is called *limiting shock strength* behaviour (Ulmschneider 1970).

Note that shock heating occurs only at the moment when the shock passes through the fluid element. Thus one might think that for waves with twice the wave period, a twofold increase of the wave amplitude compensates for the fact that the shocks occur only half as frequent. This, however, is not the case, as shock heating of weak or moderate strength depends on the third power of the wave amplitude. As seen in Fig. 2, increasing the wave period by a factor of two leads to a much larger increase of the mean temperature in a 400 s time interval. Therefore, the $P = 20$, 40, 80 and 160 s wave cases generate an increasingly steeper chromospheric temperature rise.

Given the same wave energy flux, waves with larger periods are expected to form shocks at greater heights than those with smaller periods. This is because shock formation occurs when a wave crest catches up with the preceeding wave trough, which is evidently more difficult to occur for waves with longer wave periods. In a gravitational atmosphere, shock formation is favoured by the rapid density decrease with height which, due to wave energy conservation, causes the wave amplitude to grow (see e.g. the $P = 20$ s case in Fig. 2). The motion of the wave crest relative to the wave trough, leading to the distortion of the wave profile, depends linearly on the size of the wave amplitude. Thus shock formation is greatly facilitated in a gravitational atmosphere. Therefore, one might expect that longer period waves form shocks at greater heights. This is indeed the case (see Fig. 2). The shock monitoring shows that the shock formation height is $z = 500,\ 580,\ 620,\ 640$ km for the $P = 20,\ 40,\ 80,\ 160$ s waves, respectively.

Our time-dependent wave simulations, however, show that these shock formation heights are surprisingly similar. From a factor of eight difference in wavelength, one might have expected a much larger difference in shock formation heights. The reason for this behaviour is that another effect also determines the height of shock formation. Once the first shock forms, it imparts momentum to the gas which leads to an expansion and reduces the gas density considerably. Conservation of wave energy then produces a larger wave amplitude for the next wave crest. The next shock thus forms earlier, i.e., at a lower height. For the $P = 20$ s wave, the shock formation height in the first 200 s of the calculation is found to continuously drop from $z = 1150$ km to 500 km, at which height it remains for the rest of the time (2000 s) of the calculation. The other waves show a similar behaviour: the final shock formation height is reached after $400, 900, 1100$ s for the $40, 80, 160$ s waves, respectively. As the heating and momentum deposition of the waves of greatest amplitude is largest, the effect of lowering the shock formation height due to the depletion of the gas is most pronounced for the 160 s wave, leading to a shock formation height relatively similar to that of the 20 s wave.

Let us now discuss the *exponential tube* cases (right column of Fig. 2). Surprisingly it is seen that despite of the large variation in wave period, there is no case where appreciable heating occurs. This can be understood as follows. In the exponential tube the wave energy flux, introduced at the bottom $z = z_B$, is distributed over a cross-section that increases rapidly with height (see Fig. 1). Thus, at any given height, the amplitude increase due to the density stratification is counteracted by the rapid growth of the cross-section, which keeps the increase of the wave amplitude very low. Therefore, because of the small wave amplitude, shock formation is either entirely suppressed in this tube case or the shocks remain very weak and thus produce essentially no heating.

The *wine-glass tube* cases, as displayed in the middle column of Fig. 2, show a behaviour intermediate to that of the two other tubes. Recall that due to the exponential spreading below $z_H = 400$ km and the subsequent decrease of the radius spreading rate to values close to zero near $z = 1000$ km (see Fig. 1), shock formation is much delayed and occurs above the height $z = 1000$ km. This shows that considerable heating occurs only at heights where the tube spreading is strongly reduced. It thus occurs in the constant cross-section regime where the tube has attained its maximal radius. At heights above 1000 km, the waves in the wine-glass tube show essentially the same temperature-jumps as the waves in the constant cross-section tube. This is due to the limiting shock strength behaviour of longitudinal flux tube waves, which is similar to that of acoustic waves and will be discussed in greater detail in a separate paper.

3.2. Dependence on the wave energy

Let us now consider wave calculations with increased energy fluxes. We have repeated the calculations of Fig. 2 using wave energy fluxes of $F_M = 1{\cdot}10^8$ and $1{\cdot}10^9$ erg cm^{-2}s^{-1}. As examples, Fig. 3 shows the temperature for the constant cross-section and wine-glass tube cases for waves with the period $P = 20$ s and the flux $F_M = 1 \cdot 10^9$ erg cm^{-2}s^{-1}. It was found that although the calculations of the constant cross-section and wine-glass tube cases did not present difficulties, the computations of the exponential tube cases universally failed after times of about 500 to 800 s for these higher energy fluxes. The reason for this is a property that many wave calculations display, namely the pulsational flows at great height. These oscillatory flows for large wave energies are particularly amplified in the exponential tube and lead to unrealistic situations. Fig. 3 shows in case of the constant cross-section tube (see also the case in Fig. 2) that the mean temperatures at heights greater than 1000 km are highly nonmonotonic. This is due to the fact that shock merging leads occasionally to strong shocks, which produce bumpy time-averaged temperatures and furthermore initiate the pulsational oscillations. These oscillations have also been found in pure acoustic wave computations (Rammacher & Ulmschneider 1992, Sutmann & Ulmschneider 1995). A study of pulsational flows in magnetic flux tubes is underway and will be published separately.

The increase of wave energy leads to shock formation at lower heights and consequently the number of shock merging events considerably increases over the given chromospheric height distance. Impending shock mergings are indicated by

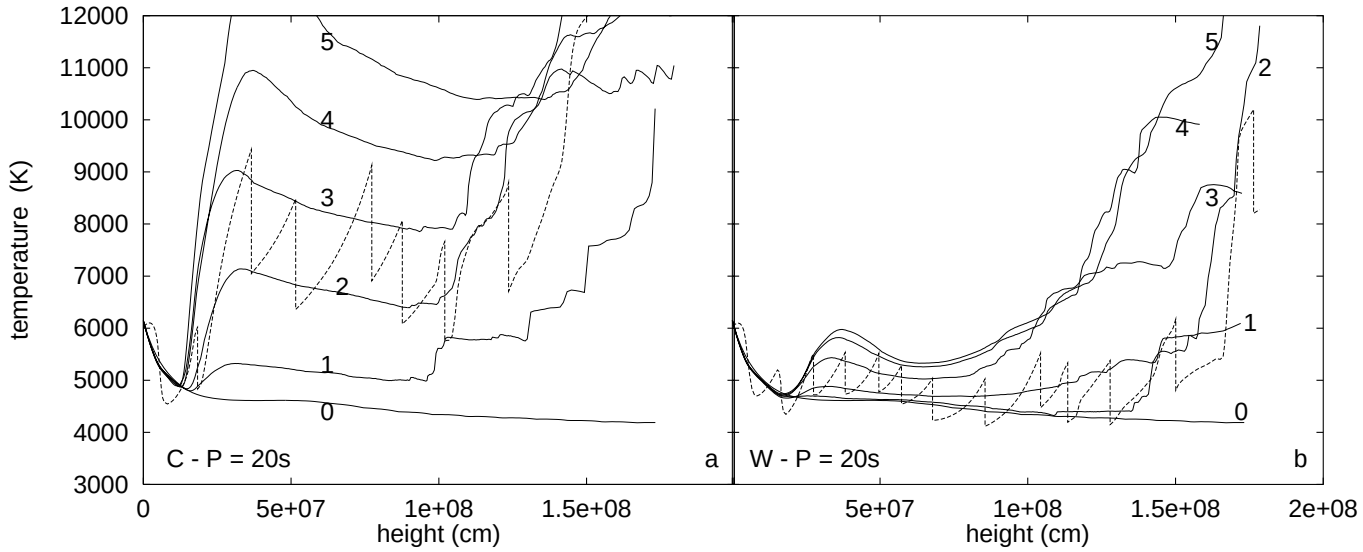

Fig. 3. Same as Fig. 2, but now for $F_M = 1 \cdot 10^9$ erg cm^{-2}s^{-1} and $P = 20$ s. Panel "a" shows the constant cross-section tube (C), panel "b" the wine-glass tube (W).

significantly different mean temperatures at the shocks (signifying different paopagation speeds) as seen at heights above 500 km in both panels of Fig. 3. Due to the exponential tube shape, the pulsational motions lead to particularly large compressions and expansions and thus generate unphysical situations as, e.g., the total internal pressure in the tube exceeds the external pressure. This behaviour is at least in part attributable to our present adiabatic treatment of the waves.

The results found in Fig. 3 are very different compared to cases of models with lower wave energy fluxes. An immediate consequence of the ten times larger initial wave amplitude (i.e., hundred times larger energy flux) is that the shock formation height is decreased to $z = 83$ and 250 km in the constant cross-section and wine-glass tube, respectively. That the shock formation height in the wine-glass tube is relatively similar to that in the constant cross-section tube (compared to a difference in shock formation height of 500 km for the tube models given in Fig. 2), is due to the fact that relative to the constant cross-section A_0, the cross-section A of the wine-glass tube has not yet increased very much at low heights (see Fig. 1).

However, between 400 and 1000 km height, the cross-section A increases rapidly, which leads to weak shock heating and consequently to small increases of the mean temperature. Above the height $z = 1000$ km, where the nearly constant cross-section region of the wine-glass tube is reached, the wave amplitude grows towards limiting strength and strong heating leads again to temperature increases similar to those in the constant cross-section tube. Thus, while the shock heating in the wine-glass tube is similar to that in the constant cross-section tube for heights where the tube has reached constant cross-section, the heating in the region of rapid spreading behaves differently. For small wave energies, shock formation occurs after this spreading zone is passed. Therefore, there is no heating in that zone. Waves with large energy produce weak shocks and therefore a region of weak shock heating in the spreading zone. The height where this weakly heated region starts depends on the initial wave energy flux.

3.3. Behaviour of the mean flow velocity

In addition to heating, shock waves also impart momentum to the gas (see Gail et al. 1990). Owing to the adiabatic treatment of the waves, these momentum additions generate flows which continuously expand the atmosphere. In an atmosphere with radiation, however, where a stable mean temperature distribution is obtained after reasonable timespans, these expansion flows eventually decrease to zero in case of short-period wave models.

In our adiabatic calculations, owing to the ever increasing temperature, these flows persist to readjust the mass distribution according to the continuously increasing density scale-height. Fig. 4 depicts these flows for the wine-glass tube and the wave periods $P = 20$ and 80 s and the flux $F_M = 1{\cdot}10^7$ erg cm^{-2}s^{-1}. It is seen that only after the constant cross-section region has been reached, do these flows become appreciable. Similarly to dissipation, these flows become larger if greater wave periods are used. Increasing the wave flux by a factor of 100 results in flows where the velocities are roughly a factor of two larger. The flows in the constant cross-section tube behave in a similar manner: they start at the region where the shocks are fully developed and are larger by a factor 2-3.

3.4. Dependence on the magnetic flux

So far, all of our tube models had the same magnetic field strength of $B_0 = 1500$ G at the bottom, $z = z_B$. We now want to consider models with $B_0 = 1000$ G. As the external gas pressure is unchanged and as we keep the same tube radius at the bottom, $r_B = 50$ km, the shapes of tubes with lower mag-

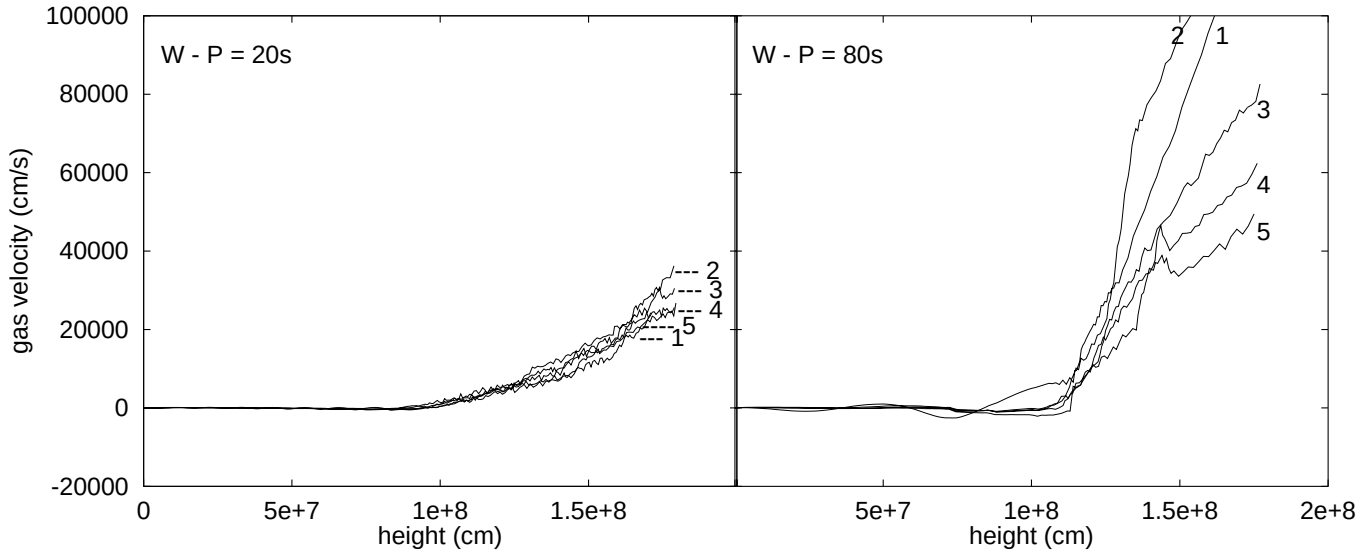

Fig. 4. Mean flow velocity induced by shock waves with $P = 20$ and 80 s and with $F_M = 1 \cdot 10^7$ erg cm^{-2}s^{-1} for the wine-glass tube (W).

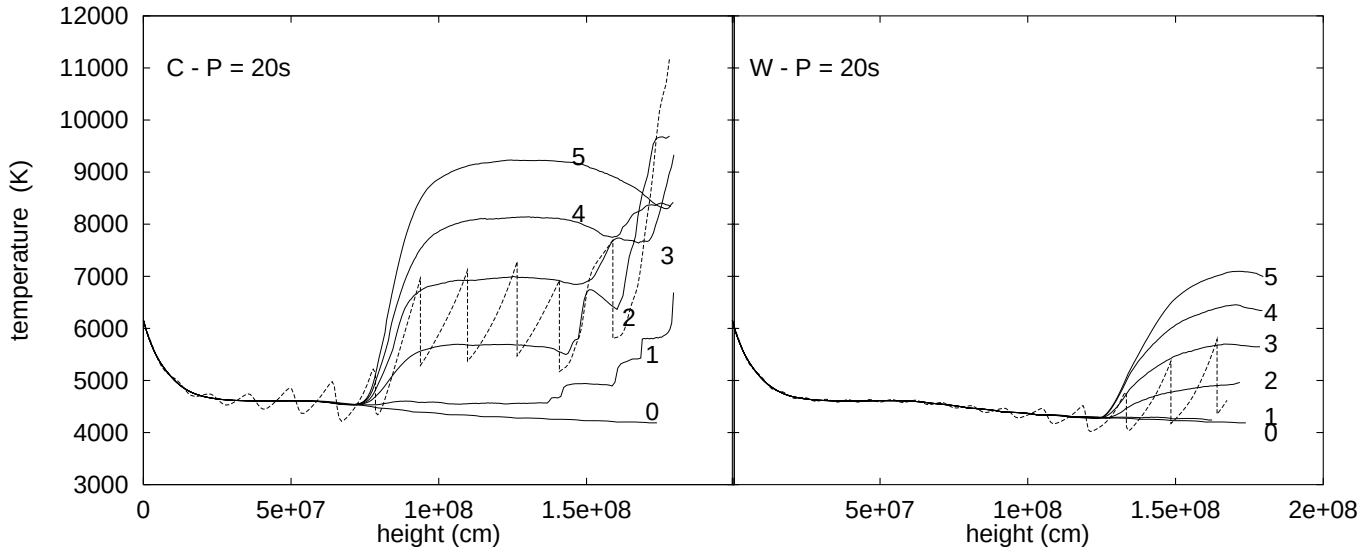

Fig. 5. Same as Fig. 2, but now for a field strength of $B = 1000$ G and waves with $P = 20$ s and $F_M = 1 \cdot 10^7$ erg cm^{-2}s^{-1} for the constant cross-section (C) and wine-glass tube (W).

netic field strength is the same as those shown in Fig. 1. For the constant cross-section and wine-glass models, Fig. 5 shows the computational results for waves of $P = 20$ s and $F_M = 1 \cdot 10^7$ erg cm^{-2}s^{-1} with the magnetic field strength $B_0 = 1000$ G.

The comparison with the corresponding cases in Fig. 2 with $B_0 = 1500$ G shows that the time development of the mean temperature in the constant cross-section case is almost identical, except that now the shock formation height is about 200 km higher. This is due to the higher gas densities in the $B_0 = 1000$ G tube. Higher gas densities lead to lower wave amplitudes u_0 (see Eq. 34), which in turn lead to a delay in the shock formation and thus to higher shock formation heights. However, as soon as the shocks become fully developed, they reach limiting strength and therefore generate essentially the same heating as found in the $B_0 = 1500$ G tube.

The wine-glass model computations show a similar effect. Here, because of the smaller initial wave amplitude, the shock formation height is increased as well, i.e., by roughly 500 km. In this model the development towards the limiting shock strength occurs over a similar distance above the shock formation height as in the corresponding high-field strength tube case of Fig. 2. Thus the rise of the mean temperature is less pronounced than at the corresponding heights of Fig. 2. In both cases, higher magnetic field strengths lead to a delay of shock formation, and in the model of the wine-glass tube also to a weakening of the shock heating. The exponential tube shows negligible shock heating, as expected.

3.5. Chromospheric emission contrast in relation to the tube models

It is well-known (Reeves et al. 1974; Solanki 1997, private communication) that at the height of O VI formation, the network emission still shows a high contrast, similar to that at lower layers where the Lyman continuum and the C II line are formed. This is puzzling because this contrast occurs at heights where the magnetic field has long formed a canopy and has filled out all the available space. The great differences in the heating properties of tubes of different geometry as described above provides a possibility to explain this persistent height-independent contrast, although our results need to be updated by considering models with radiative damping. In the center of the network one has tubes of (nearly) constant cross-section and at the network boundary one has (nearly) exponential-type tubes. The concentration of the heating in the network center is thus nicely contrasted to the weak or negligible heating in regions of the network boundary, a behaviour that is consistent with the above-mentioned observation.

4. Conclusions

We introduced various adiabatic longitudinal monochromatic waves by means of a piston into magnetic flux tubes of different geometries and monitored the formation and propagation of shocks and the heating by shock dissipation. We found the following results:

1. Exponential tubes have little or no shock heating owing to the rapid increase of the cross-section, which counteracts the wave amplitude growth due to the density stratification. This agrees well with the fact that the chromospheric network emission retains its strong contrast even above the canopy height.

2. While constant cross-section tubes are efficiently heated, the heating in wine-glass tubes depends on the extent of the zone of rapid cross-section spreading. In this zone shock formation is delayed and shock heating, if present, is weak. Above that zone shock heating is equivalent to that in constant cross-section tubes.

3. Greater wave periods lead to stronger heating, an effect particularly evident at large atmospheric heights. Greater wave periods also lead to increased outflow velocities due to the increase in wave pressure.

4. In tubes with lower field strength the height of shock formation is increased. Above that height, constant cross-section tubes are efficiently heated. At a given height wine-glass tubes are less efficiently heated than tubes of higher magnetic field strength.

Acknowledgements. We are grateful to Deutsche Forschungsgemeinschaft and to NATO for support. This work was also partially funded by the NASA Astrophysics Theory Program (grant number NAG5-3027) to the University of Alabama in Huntsville. We also thank S. Solanki for helpful comments on the manuscript.

References

Buchholz B., Ulmschneider P., 1994. In: Caillault J.-P. (ed.) Cool Stars, Stellar Systems, and the Sun XIII. ASP Conf. Series 64, p. 363
Buchholz B., Ulmschneider P., Cuntz M., 1998, ApJ, 494, 700
Carlsson M., Stein R.F., 1992, ApJ, 397, L59
Cuntz M., Rammacher W., Ulmschneider P., 1994, ApJ 432, 690
Cuntz M., Ulmschneider P., Musielak Z.E., 1998, ApJ 493, L117
Defouw R.J., 1976, ApJ 209, 266
Edwin P.M., Roberts B., 1983, Solar Phys. 88, 179
Gail H.-P., Cuntz M., Ulmschneider P., 1990, A&A 234, 359
Hasan S.S., van Ballegooijen A.A., 1997, In: Donahue R.A., Bookbinder J.A. (eds.) Cool Stars, Stellar Systems, and the Sun X. Abstract Edition
Herbold G., Ulmschneider P., Spruit H.C., Rosner R., 1985, A&A 145, 157
Hollweg J.V., 1986. In: Buti B. (ed.) Advances in Space Plasma Physics. World Scientific, Singapore, p. 77
Hollweg J.V., 1990. In: Russell C.T., Priest E.R., Lee L.C. (eds.) Physics of Magnetic Flux Ropes. AGU, Washington, Geophys. Mono. 58, p. 23
Huang P., 1996, Phys. Plasmas 3, 2579
Huang P., Musielak Z.E., Ulmschneider P., 1995, A&A 297, 579
Judge P.G., Hansteen V., Wiskøl Ø., et al., 1998, ApJ, in press
Linsky J.L., 1980, ARA&A 18, 439
Musielak Z.E., Rosner R., Ulmschneider P., 1989, ApJ 337, 470
Musielak Z.E., Rosner R., Stein R.F., Ulmschneider P., 1994, ApJ 423, 474
Musielak Z.E., Rosner R., Gail H.-P., Ulmschneider P., 1995, ApJ 448, 865
Narain U., Ulmschneider P., 1990, Space Sci. Rev. 54, 377
Narain U., Ulmschneider P., 1996, Space Sci. Rev. 75, 453
Parker E.N., 1979, Cosmical Magnetic Fields, Clarendon Press, Oxford, Chap. 8
Rae I.C., Roberts B., 1982, ApJ 256, 761
Rammacher W., Ulmschneider P., 1992, A&A 253, 586
Reeves E.M., Foukal P.V., Huber M.C.E. et al., 1974, ApJ 188, L27
Roberts B., 1981. In: Cram L.E., Thomas J.H. (eds.) Physics of Sunspots. Sacramento Peak Observatory, Sunspot, New Mexico, p. 369
Roberts B., 1983, Solar Phys. 87, 77
Roberts B., 1991. In: Priest E.R., Hood A.W. (eds.) Advances in Solar System Magnetohydrodynamics. Cambridge University Press, Cambridge, p. 105
Roberts B., Ulmschneider P., 1997. In: Simett G.M., Alissandrakis C.E., Vlahos L. (eds.) Solar and Heliospheric Plasma Physics. Springer, Berlin, p. 75
Roberts B., Webb A.R., 1978, Solar Phys. 56, 5
Roberts B., Webb A.R., 1979, Solar Phys. 64, 77
Ryutova M.P., 1990. In: Priest E.R., Krishan V. (eds.) Basic Plasma Processes in the Sun. Kluwer, Dordrecht, p. 175
Schüssler M., 1991, Geophys. Astrophys. Fluid Dynamics 62, 271
Solanki S.K., 1990. In: Stenflo J.O. (ed.) Solar Photosphere: Structure, Convection and Magnetic Fields. Reidel, Dordrecht, IAU Symp. 138, p. 103
Solanki S.K., 1993, Space Sci. Rev. 63, 1
Solanki S.K., 1997. In: Simett G.M., Alissandrakis C.E., Vlahos L. (eds.) Solar and Heliospheric Plasma Physics. Springer, Berlin, p. 49
Spruit H.C., 1981a. In: Jordan S. (ed.) The Sun as a Star. NASA, Washington, NASA SP-450, p. 385
Spruit H.C., 1981b, A&A 98, 155

Spruit H.C., 1982, Solar Phys. 75, 3
Spruit H.C., Roberts, B., 1983, Nature 304, 401
Stenflo J.O., 1978, Rep. Progr. Phys. 41, 865
Stenflo J.O., 1989, A&AR 1, 3
Stenflo J.O., 1994. In: Schüssler M., Schmidt W. (eds.) Solar Magnetic Fields. Cambridge University Press, Cambridge, p. 301
Sutmann G., Ulmschneider P., 1995, A&A 294, 241
Thomas J.H., 1985, In: Schmidt H.U. (ed.) Theoretical Problems in High Resolution Solar Physics. Max Planck Institute, Munich, MPA 212, p. 126
Ulmschneider P., 1970, Solar Phys. 12, 403
Ulmschneider P., Musielak Z.E., 1998, A&A, in press
Vaiana G.S., Cassinelli J.P., Fabbiano G. et al., 1981, ApJ 245, 163
Wang H., Tang F., Zirin H., Wang J., 1996, Solar Phys. 165, 233
Webb A.R., Roberts B., 1980, Solar Phys. 68, 87
Wentzel D.G., 1979, A&A 76, 20
Wilson P., 1979, A&A 71, 9
Wilson P., 1980, ApJ 237, 1008
Wilson P., 1981, ApJ 251, 756
Wood B.E., Linsky J.L., Ayres T.R., 1997, ApJ 478, 745
Zhugzhda Y., Bromm V., Ulmschneider P., 1995, A&A 300, 302
Ziegler U., Ulmschneider P., 1997a, A&A 324, 417
Ziegler U., Ulmschneider P., 1997b, A&A 327, 854
Zwaan C., 1978, Solar Phys. 60, 213